

Point sources in the MAP sky maps

Elena Pierpaoli ¹

ABSTRACT

We discuss point sources foregrounds for the MAP experiment. We consider several possible strategies for removing them and we assess how the statistics of the CMB signal are affected by the residual sources. Assuming a power law distribution for the point sources, we propose a method aimed to determine the slope of the distribution from the analysis of the moments of the observed maps. The same method allows for a determination of the underlying CMB variance. We conclude that the best strategy for point sources finding is the simultaneous thresholding of the filtered map at all frequencies, with a relatively low threshold. With this strategy, we expect to find 70 (95)% of the sources above 3 (4) σ . Assuming the most conservative case for point sources detection, the recovered slope of the point sources distribution is 2.55 ± 0.15 , for a fiducial $n = 2.5$ value. The recovered CMB plus noise map variance is within 0.2% from the real one, with a standard deviation of 0.31%, while Cosmic variance contributes 2.2% to the same CMB plus noise map.

Subject headings: cosmic microwave background: extra galactic foregrounds

1. Introduction

The upcoming cosmic microwave background (CMB) experiments MAP (Bennet et al., 2003) and Planck (Mandolesi et al., 2002) face the ambitious task of determining several cosmological parameter with a high level of accuracy. Their ambitious goals require the ability in cleaning the maps from the galactic and extra-galactic foregrounds (Refregier and Spergel, 2000). In this paper we address the issue of the possible performance the satellite MAP can have in subtracting a specific extra-galactic foreground, that is the point sources.

Point sources cannot be avoided by sky cuts, and are the main source of uncertainty at small angular scale where, even when all bright sources are identified and subtracted, their residual contribution may dominate over Cosmic variance. For example, point sources have

¹Physics Department and Astronomy Department, Princeton University, Princeton, NJ, 08544

been the main foreground issue for the CBI experiment (Myers et al., 2002), where they have been the only foreground explicitly modeled and considered in the overall likelihood.

Two approaches are commonly adopted for point sources identification: *ii)* the use of exiting point sources catalogs; *i)* the direct search on the data map or on a filtered version of it. In this paper we will discuss the latter.

The simplest version of the direct search consists in straight thresholding of the data. This naive approach only finds very bright sources. An improved version consists in first filtering the data with an appropriate filter that maximizes the signal of the point source peak with respect to the *noise* intended as CMB signal plus instrumental noise (Tegmark and de Olivera–Costa 1998). Here the knowledge of the CMB and the instrumental power spectra are assumed (see also Chiang et al. 2002 for a different approach). Alternatively, it is possible to look for point sources in a map obtained by subtraction of two given frequency maps. The thresholding procedure selects from these maps a subsample of pixels that are more likely to be contaminated by point sources. This subsample may be used as the point sources catalog (if the threshold is high enough to avoid fake detections) or as a useful template for further investigations with alternative techniques. This subsample is particularly useful for point sources detection in all sky experiments like MAP and Planck, whose maps contain a large number of pixels. In this paper we discuss the performances of the thresholding technique when applied to an experiment with the characteristics of MAP. More specifically, for each method described above we discuss which fraction of the sources are selected after thresholding the frequency maps at different levels and how many pixel in the map are selected by the same procedure. We suggest a method aimed to maximize the former and minimize the latter.

Alternative techniques have been proposed in the literature. For example, Naselsky et al. (2002) proposed a generalization of the filtering method to multi-frequency experiments, claiming an increased signal to noise ratio when filtering an appropriate linear combination of the observed maps. A possible limitation of this method is the needed assumption on the point source frequency behavior.

Maxican–hat wavelets have also been applied in subtracting the point sources (Cayon et al. 2000, Vielva et al. 2001a), alone or in conjunction with maximum–entropy (Vielva et al. 2001b). This technique applies to single frequency maps, and performs similarly to the filtering method. In fact, the filters used in the two methods, although derived with different prescriptions, end up to be similar.

We then address the issue of the statistical contamination of the residual sources in the CMB map, estimating the accuracy with which the CMB variance can be recovered if

all sources above a certain threshold are removed from the observed map. We then briefly discuss the impact of residual point sources on the power spectrum.

We show how the moments of the observed map point distribution function can be used to infer characteristics of the point sources population, namely the slope of the point sources flux distribution.

The paper is organized as follows: in section 2 we present the characteristics of the simulation; in section 3 we present the results obtained, that is the efficiency in finding point sources (3.1), the impact of the residual signal on the statistics of the CMB map and power spectrum and the performance in the determination of the slope of the point sources distribution (3.2, 3.3). Section 4 is dedicated to the conclusions.

2. Simulations

We simulate CMB sky maps with the characteristics of the MAP experiment (see tab. 1). For this purpose we use a cold dark matter power spectrum, and uniform Gaussian noise.

Simulations were performed in the Healpix pixellization scheme (5), with resolution $N=256$. The typical pixel side is 0.2 degrees, which is comparable to the highest resolution of the experiment.

As for the point sources, we consider the following flux dependence:

$$d\mathcal{N}(S) = A S^{-n} dS \quad (1)$$

with $n = 2.5$ (expected values of n range from 1.5 to 2.5). We consider two different normalizations, which amount to have 178 or 356 sources respectively above 1 Jy at 90 GHz.

Table 1: The characteristics of the MAP experiment: column one is the frequency of observation, column two is the FWHM of the beam in degrees, column three (four) is the expected noise standard deviation for 2 years (six months) observation and for a 0.3×0.3 degrees pixel in μK .

ν (GHz)	θ_{FWHM}	σ_n (μK , 2yrs)	σ_n (μK , 6mo.)
22	0.89	35	70
30	0.646	35	70
40	0.504	35	70
60	0.312	35	70
90	0.214	35	70

These normalizations correspond approximately with the numbers proposed by Holdaway et al. (1994) and Toffolatti et al. (1998) respectively. We present most results are presented in the highest normalization case, while we mainly use the lower for testing.

At low fluxes the power law in eq. 1 is expected to break down, the exact flux at which this happens and the shape of the distribution at lower fluxes is unknown. We take this into account by simulating only sources with flux above $S_{min} = 0.01$ Jy at 90 GHz. We then extrapolate the 90 GHz simulated sources to lower frequencies assuming an approximately flat spectrum:

$$S(\nu) \propto \nu^{-\gamma} \quad (2)$$

with γ randomly chosen in the range $[-0.3, 0.3]$.

We convolve the point sources maps with the appropriate beam before summing it to the CMB plus noise (CMBn) ones. We do not introduce other foregrounds in our modeling, therefore the estimates we make should be considered to hold for regions that have a negligible contamination of other foregrounds.

We have about 5540 sources in our catalog with the lower normalization, and the double with the higher. In table 2 we show how their flux compares to the standard deviation of the CMBn map at 90 GHz.

3. Results

In this section we present our results. In sec. (3.1) we analyze and compare different methods for point sources finding. In sec. (3.2) we use the statistics of the observed map in order to assess the underlying CMBn map variance and the characteristics of the point sources distribution. Finally, in sec. (3.3) we show the impact of residual point sources on the power spectrum.

3.1. Point sources identification

In this section we compare three techniques for point sources identification. Namely, we perform a thresholding on the following maps: *i*the raw data (method I); *ii* the maps obtained after applying the filter introduced by Tegmark et al. (1998) (method II); a map obtained by the subtraction of two maps at different frequencies (method III).

More specifically, in order to apply method II we convolve the observed image in each

Table 2: The distribution of simulated sources fluxes at 90 GHz with respect to the standard deviation in the CMB plus noise (CMBn) map. The first column is the cut in units of σ_{CMBn} , the second and third columns are respectively the number and the fraction of simulated sources within that range. These numbers correspond to the higher normalization of the point sources distribution.

σ_{CMBn} threshold	N_s	F_s
< 1	7548	0.674
1 – 2	2336	0.209
2 – 3	617	0.055
3 – 4	238	0.021
4 – 5	135	0.012
5 – 6	69	0.006
6 – 7	48	0.004
7 – 8	40	0.003
8 – 9	21	0.0019
9 – 10	25	0.002
10 – 11	13	0.001
11 – 12	9	0.001
> 12	92	0.008

given frequency with a window function whose spherical harmonics coefficients are:

$$W(l) = \frac{b(l)}{b(l)^2 C(l) + C_{noise}(l)} \quad (3)$$

where $b(l)$ is the spherical harmonics of the beam and $C(l)$ and $C_{noise}(l)$ are the power spectra of the CMB and noise respectively. This filtering has the advantage of subtracting the background and lowering the noise. As a result, it reduces the bias one may have in thresholding the data directly, where sources of the same intensity are less (more) likely to be detected if they sit in a CMB valley (hill).

In order to apply method III we deconvolve the 90 GHz map, and then we subtract it from each other frequency map after convolving it with the beam of the experiment at that frequency. This strategy is aimed to subtract the CMB signal. The potential problem is the increased noise in the output maps.

After filtering the data or combining the observed maps as explained above, point sources candidates are selected by thresholding the output maps and retaining all pixels above a given threshold. A candidate pixel can be confirmed as a point source center by looking at the radial profile of the map around it, or at the frequency dependence of that particular pixel in all frequency maps. This procedure is necessary when dealing with real data, and it allows to produce a catalog of objects with a certain likelihood of being a point source. The detection probability will ultimately depend upon the likelihood method applied and the modeling of the source considered. Clearly, point sources that didn't make it above the threshold are certainly not going to be detected. While lowering the threshold allows for more sources to get into the selected set of pixel, it would also allow for a greater number of pixels not associated with point sources to enter the selected sample. It is therefore important to decide which method retains the greatest number of sources locations among the selected pixels and compare it to the total number of pixels selected at any given threshold. By minimizing the number of pixel selected while maximizing the one containing the point sources centers we have tentative point sources catalog that can be used for efficient point sources confirmation with alternative methods.

We proceed by comparing method I and II first. We filtered each frequency map independently with the filter in eq. 3, and performed a thresholding the filtered map and of the raw data at different levels (parametrized by the standard deviation of the map in hand σ_{thr}). We then counted the point sources found above a given level ², and how many pixels are in the subsample.

²We consider a source to be found if the pixel corresponding to its center has an intensity above the threshold

In figs. 1 and 2 we show the performance of the two methods in finding the point sources. The plot in fig. 1 reports the ratio between the fraction of point sources found F_{sf} with respect to the fraction of pixel selected F_{ap} as a function of the threshold σ_{thr} . The frequency where source finding is more efficient is 90 GHz. We note that in the filtered map there is a big increase in efficiency for σ_{thr} between 1 and 3 (this value is shifted between 2 and 4 for the data map). Looking at fig. 2 it is clear that the threshold on the 90 GHz map is set at $\sigma_{thr} = 2$ only about 20% of the total sources can be found.

Lowering the threshold at $1\sigma_{thr}$ allows to detect about 1/2 of the sources, including all sources above 3σ (see fig. 3) and 85% of sources above 2σ . However, one would still be left with about 10% of the total number of pixel to analyze (fig. 2, upper left panel). This problem can be avoided by selecting the pixels according to whether or not they are above a certain threshold at all frequencies. The bottom right panel in fig. 2 shows that if one considers pixels with signal above $0.5 - 1\sigma_{thr}$ at all frequencies, one may still find 20 – 50% of all sources with less pixels to analyze. The ratio between the number of pixels occupied by point sources centers and the number of pixels above the threshold (R_{occ} ; dashed line in fig. 2) ranges between 0.5 and 0.95, while in order to get a similar amount of sources from the 90 GHz map alone that ratio is 0.05 – 0.2.

In the same thresholding range, if we considered all the observed maps instead of the filtered ones we would still be able to find 0.2 – 0.4 of the total number of sources, but with a much noisier signal: the ratio R_{occ} would be 0.15 – 0.20.

In fig. 3 we report the fraction of sources found above a certain threshold in all filtered maps as a function of source intensity. If σ_{thr} is chosen to be one, 95% of sources above 4σ and 70% above 3σ can be found. Due to the steepness of the curves, lowering the threshold to 0.5σ would imply the possible detection of 90% of sources above 3σ and 65% above 2σ . When dealing with the real map, however, there is the additional complication of confirming the point sources by looking at their profile in the map. This procedure is likely to be more difficult for weaker sources. The number estimated here are therefore to be considered optimistic for weak sources.

When analyzing the maps obtained as differences of two frequency maps (method III), we find different results according to the frequency considered. The efficiency of point sources finding on the (60 – 90) GHz map is very low, the fraction of point sources found being equal to the fraction of pixels analyzed for any threshold. When maps at lower frequencies are considered, the performance of this method is similar to the filtering one (method II). However, the combined information from different frequencies is lower because in practice this procedure gives up two frequency maps.

We conclude that the best strategy consists in using the combined information from the filtering method (method II), with a threshold $0.5 - 1 \sigma_{thr}$.

Note that the procedure proposed does not assume any particular frequency dependence for the point sources. It just exploits the fact that point sources are expected to be in the same locations in the different frequency maps, while the peaks in the noise distribution are uncorrelated between frequency maps.

The present analysis was based on some assumptions implicit in the simulations, like the pixel size or the frequency dependence of the point sources. As for the pixel size, we assume the biggest possible considering the highest experiment resolution. If we chose to perform a higher resolution simulation the noise variance would increase, while the signal from point sources would remain the same. Since method II performs a convolution of the map with a window function that has a characteristic smoothing scale of the order of the beam size at that frequency, using a finer resolution wouldn't change the performance. In methods I and II there would be an increase of spurious detections at any given threshold due to the higher pixel noise, resulting in a less efficient point sources finding. Given our conclusion on the preferred method, we don't investigate this issue any further.

As for the frequency dependence of point sources, the approximately flat spectra sources we simulated seem to fit the majority of radio sources (Sokasian et al. 2001). The Rayleigh–Jeans temperature fluctuation produced by point sources scales as $\Delta T = S(\nu)\Theta_{FWHM}^{-2}\nu^{-2}$, and since for MAP we have $\Theta_{FWHM} \propto \nu^{-1}$ there is no obvious frequency map where to look for flat spectrum sources. Should future observations suggest that a considerable fraction of sources show significant departures from this frequency dependence, a different strategy might be needed. In particular, if the spectra show a bump in the frequency range of interest, there might be a preferred frequency map, different from the 90 GHz one, for point sources detection. The method presented here is however not dependent on the point sources spectrum, and can in principle be investigated with different simulations.

3.2. Using moments to determine residual point sources contribution

After having identified and subtracted the bright sources, the remaining ones still affect the real space statistics of the CMB that we want to measure. We shall use this dependence in order to infer both properties of the point sources distribution and the expected variance of the CMBn point distribution function.

Having assumed Gaussian fluctuations, we expect the point distribution function of the

CMB signal to be completely described by its variance. For a full sky experiment we have:

$$\sigma_{CMB}^2 = \sum_l \frac{2}{4\pi} \frac{l+1}{l} C(l) b^2(l). \quad (4)$$

While an unbiased estimator for this quantity exists, Cosmic variance sets a limit to the precision with which the variance is determined:

$$var(\sigma_{CMB}^2) = \sum_l \frac{2}{(4\pi)^2} \frac{(l+1)}{l} C^2(l) b^4(l). \quad (5)$$

In the specific CDM case we are adopting here and for the beam of the 90 GHz map, we have:

$$\sqrt{(var(\sigma_{CMB}^2))}/\sigma_{CMB}^2 = 3.0\%. \quad (6)$$

Given the additional contribution of the noise (for our pixellization and 2 years of data), the Cosmic variance is expected to be 2.2% of the CMB plus noise signal ($\sigma_{CMBn}^2 = \sigma_{CMB}^2 + \sigma_{noise}^2$).

Faint point sources contaminate the map rendering the CMB+noise statistics non-Gaussian. Estimators of non-Gaussianity may rely on asymmetries of the point distribution function and the study of its moments (Rubin–Martin & Sunyaev, 2002), or on the study of the bispectrum and trispectrum in Fourier space (Komatsu et al 2001).

In this work we concentrate on the first four moments of the point distribution function of the map after sources subtraction. On the 90 GHz map we performed a progressive subtraction of point sources above a certain threshold σ_{cut} (expressed in units of σ_{CMBn}). All pixels in a ring of radius of 1 FWHM from the point source location were removed from the map in order to avoid residual signal from the convolution process.

In figs. 4 we show, for a particular map, how the various moments are affected by the remaining point sources. Although bright sources are rare, their impact on the statistics of the map is most relevant. For example, in the realistic case that all sources above $4\sigma_{CMBn}$ are removed, the estimated variance of the cleaned map would be within 2% of σ_{CMBn}^2 . This means that residual point sources potentially affect the final distribution inducing an error on the variance comparable to the Cosmic variance.

The other relevant feature of fig. 4 is the shape of the curves, which is linked to the characteristics of the point sources distribution. In the following we will discuss how well it is possible to determine such distribution and the variance of the CMB by looking at the moments of the maps. The moments plotted here are non-centered, that is they are calculated as: $\langle x^\beta \rangle = \int x^\beta \mathcal{N} dx$, where \mathcal{N} is the normalized pixel distribution. For a

Gaussian field with zero mean, as the simulated CMBn map is, we would expect $\langle x \rangle = 0$, $\langle x^2 \rangle = \sigma^2$, $\langle x^3 \rangle = 0$, $\langle x^4 \rangle = 3\sigma^4$. In reality, the CMBn map itself deviates from this formulae because of Cosmic variance, so that the Gaussianity hypothesis cannot be fully exploited. In the following we assumed $\langle x \rangle = 0$ and $\langle x^4 \rangle = 3\langle x^2 \rangle$, but put no constraints on $\langle x^3 \rangle$. The final map is a sum of the CMBn map (x) and the point sources (e): $x_T = x + e$. Given the assumptions above, the moments of the total map can be expressed in terms of moments of x and e as follows:

$$\langle x_T \rangle = \langle e \rangle \quad (7)$$

$$\langle x_T^2 \rangle = \langle x^2 \rangle + \langle e^2 \rangle \quad (8)$$

$$\langle x_T^3 \rangle = \langle x^3 \rangle + \langle e^3 \rangle + 3\langle x^2 \rangle \langle e \rangle \quad (9)$$

$$\langle x_T \rangle = 3\langle x^2 \rangle (\langle x^2 \rangle + 2\langle e^2 \rangle) + \langle e^4 \rangle \quad (10)$$

$$(11)$$

where e is a function of the intensity of the sources removed: $e(\sigma_{cut}) = \int_{S_{min}}^{S_{cut}} \mathcal{N}_{pts} dx$, with $S_{cut} = \sigma_{cut} \sigma_{CMBn}$.

Any given moment is therefore a function of the slope n , the normalization A and the minimum flux of the sources S_{min} , none of which is supposed to be known a priori. We performed 100 simulations of point sources map and added them to a noisy CMB one. For any given simulated map, we calculated the first four moments as a function of σ_{cut} . We then fixed n and performed a simultaneous fit to all moments using the formulas in eq. (11). As a conservative approach, we considered to be able to detect only sources above $4\sigma_{CMBn}$, and therefore considered to know the curves in fig. 4 only for $\sigma_{cut} \geq 4$. The parameters of the fit were: $\langle x^2 \rangle, \langle x^3 \rangle, A$ and S_{min} , and the likelihood was simply the sum over all moments and all points of the percentage difference of the fit to the data. We then selected the n value which minimized the likelihood, and its associated parameters at the best fit.

In figs. (5) and (6) and we show the histograms for the n values found and for the assessed σ_{CMBn} . As for the n value, the estimated mean and standard deviation are: $n = 2.55 \pm 0.15$. The significant standard deviation of the distribution is due to the fact that there is degeneracy between the parameters, in particular between n and A . The best fit theoretical curves for a fixed n are indistinguishable, so that one should resort to other methods to have a more precise n estimate. An alternative method, not investigated here, could consist in fitting the positive tail of the observed distribution, in the region where the CMBn contribution is expected to be negligible.

On the other hand, the shape of the underlying theoretical curves is very well constrained. As a result, the estimated value of the CMBn map variance (σ_{est}^2) is very close to

the true one: $(\sigma_{est}^2 - \sigma_{CMBn}^2)/\sigma_{CMBn}^2 = -0.22\% \pm 0.31\%$. Knowing the noise properties of the instrument, we are therefore confident that we can estimate the variance of our underlying CMB map with a precision that is far below Cosmic variance. In fig. (6) we also note that if we actually knew the precise true n value, our estimate for the variance would have been $(\sigma_{est}^2 - \sigma_{CMBn}^2)/\sigma_{CMBn}^2 = 0.11\% \pm 0.15\%$.

These results are dependent on the fact that all curves are fitted simultaneously and that the second and fourth moment for the CMB follow the Gaussian hypothesis. Fitting the variance curve only doesn't allow neither a good determination of the spectral index n nor of the CMBn variance. When imposing that all curves are fitted simultaneously, improved results are obtained only if we impose that the extrapolated values for the second and fourth moments follow what one would expect for a Gaussian distribution.

The value of σ_{CMBn} depends on the pixel noise which in turn is a function of the pixel size assumed. Given any initial finer pixellization, it is possible to rebin the map to this resolution without loss of cosmological information. The present procedure can then be applied.

3.3. The impact of point sources on the power spectrum

In this section we show the impact of the point sources on the power spectrum, computed as $C_l = \sum_m |a_{lm}|^2$ where a_{lm} are the spherical harmonics of the map. We applied the procedure to the observed map (CMBn plus point sources) and then to the observed map where sources above a specific threshold have been subtracted. In fig.(7) we show, for a particular 90 GHz map, the difference between the power spectrum of the observed map and the underlying CMBn one. Point sources contaminate the power spectrum at 20% level at $l \simeq 200$. In fig.(8) we plot, for some particular l 's, the percentage difference between the CMBn power spectrum and the one obtained from the maps where sources above a threshold σ_{cut} have been subtracted. Bright sources have the greatest impact on the power spectrum. Subtracting sources above 12σ , for example, brings the power spectrum from more than 100% to only 9% away from the CMBn one at $l=400$. Progressively subtracting fainter sources have a greater impact on the higher l 's. At $l \simeq 200$, the impact of point sources is about 2% quite independently from σ_{cut} (fig. 8). If all sources above 4σ are subtracted from the map, the power spectrum is overestimated by about 2% at $l = 200$ and about 15% at $l=400$.

4. Conclusions

We investigated the problem of point sources subtraction from the observed MAP multi-frequency maps.

First we analyzed possible strategies for point sources finding without the help of external maps. We found that the best strategy consists in applying the linear filtering in eq. 3 to each frequency independently, cutting the maps with a relative low threshold ($0.5 - 1\sigma_{thr}$) and then considering only the pixels that satisfy this constraint in all maps. This method outperforms similar strategies applied to observed maps and to maps obtained by subtraction of two frequencies. With this strategy we may expect to find 95% of sources above 4σ and 70% above 3σ , as a conservative estimate.

Assuming that the brightest sources are going to be found, we addressed the issue of how statistics is affected by the residual sources in the map. If all sources above 4σ are found the variance of the CMB map is recovered within 2%. We used the information from the first four moments of the map to infer the variance of the CMB plus noise map and the slope of the point sources distribution. The results are summarized in figs. 5 and 6. Extrapolating the variance curve to null source contribution (0σ) allows to determine the variance of the *CMB* plus noise map within $-0.2 \pm 0.3\%$. This value should be compared with the ratio of Cosmic variance to the CMBn one, which is about 2.2% for the CDM case treated here. The same strategy allows for a determination of the spectral index of the point sources distribution. For a fiducial $n = 2.5$ value, we find $n = 2.55 \pm 0.15$, where the significant spread is due to a degeneracy with the normalization A .

These results are obtained in the approximation of null contribution from other foregrounds. While this is likely to be the case close to the galactic pole, it may not hold near the plane. It is always possible to apply this method to submaps of the sky, although the lower number of bright sources would probably reduce the performance.

E.P. is supported by NASA grant NAG5-11489 and NAG5-10811. E.P. thanks David Spergel for useful discussions, the anonymous referee for comments and the Aspen Center for Physics for hospitality during the preparation of this work.

REFERENCES

Bennet et al., ApJ in press, astro-ph/0301160
Mandolesi, N. et al., AIP Conf.Proc., 2002, 616, 193

Cayon, L., et al., 2000, MNRAS, 315, 755

Chiang, L.Y., Jorgensen, H.E., Naselsky, I.P., Naselsky, P.D., Novikov, I.D., Christensen, P.R., 2002, MNRAS335, 1054

Healpix web page, <http://www.eso.org/science/healpix>

Holdaway M.A., Owen, F.N., Rupen, M.P., 1994, NRAO report, unpublished.

Komatsu, E., et al., 2002, ApJ, 566, 19

Myers, S.T., et al., astro-ph/0205385

Naselsky, P., Novikov, D., Silk, J., 2002, MNRAS, 335, 1050

Refregier, A., Spergel, D.N., 2000, ApJ531, 31

Rubino–Martin, J.A., Sunyaev, R.A., 2002, astro-ph/0211430

Sokasian, A., Gawiser, E., Smoot, G.F., 2001, ApJ, 562, 88

Tegmark, M., de Olivera–Costa, A., 1998, ApJ, 500, 83

Toffolatti et al., 1998, MNRAS, 297, 117

Vielva, P., Martinez–Gonzales, E., Cayon, L., Diego, J.M., Sanz, J.L., Toffolatti, L., 2001, MNRAS, 326, 181

Vielva, P., et al., 2001b, MNRAS, 328, 1

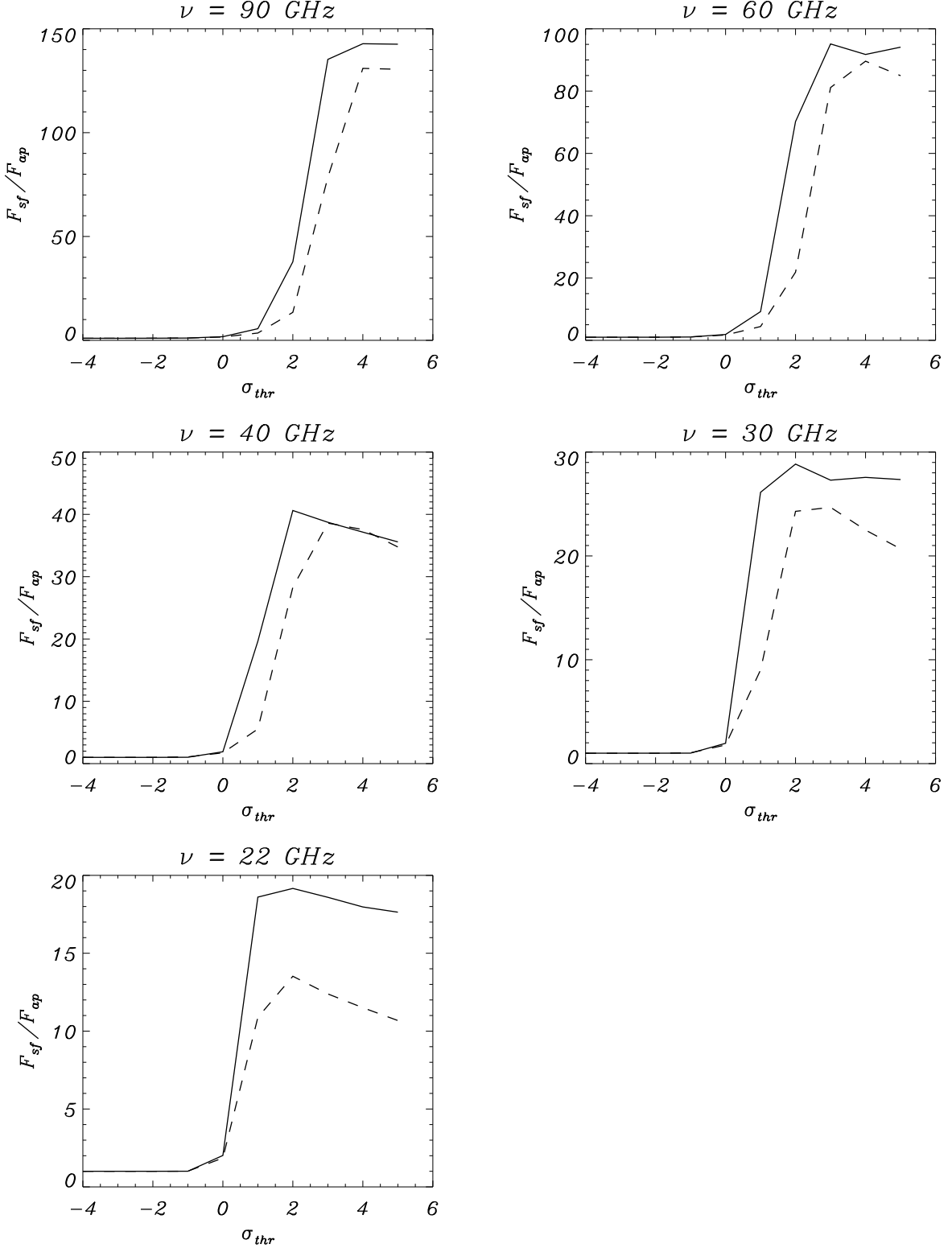


Fig. 1.— Efficiency of the thresholding procedure. The y axes shows the fraction of point sources found over the fraction of pixels in the map above threshold σ_{thr} . The solid line corresponds to the filtered map (method II) while the dashed to the observed data map. σ_{thr} is the standard deviation of the map under analysis.

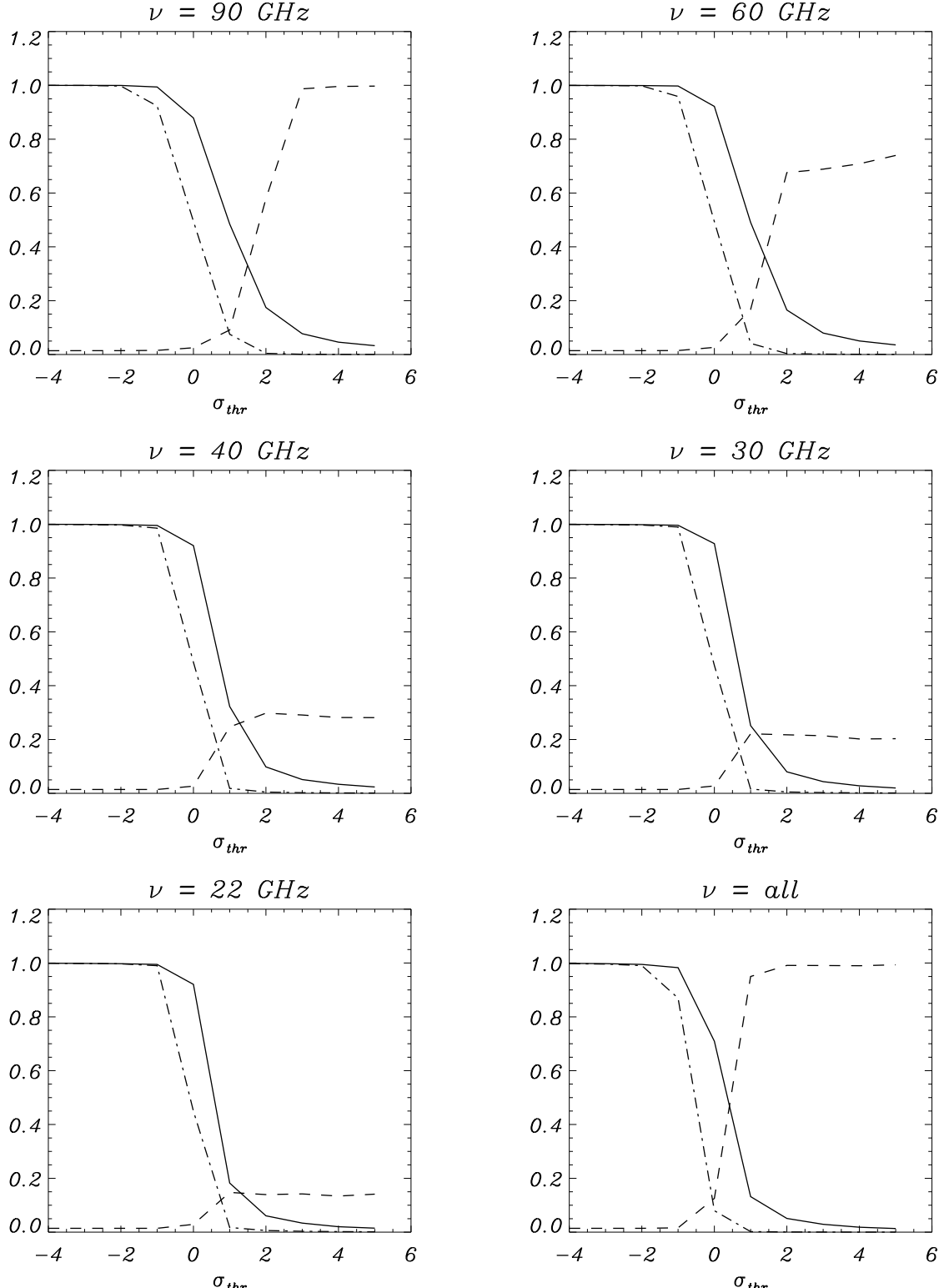


Fig. 2.— Performance of the filtering method (method II). Various fractions are plot as a function of the threshold applied (in units of the filtered map standard deviation). Solid line: fraction of sources found. Dashed line: number of pixel containing point sources over number pixel considered. Dot-dashed line: fraction of pixel considered over total number of pixel.

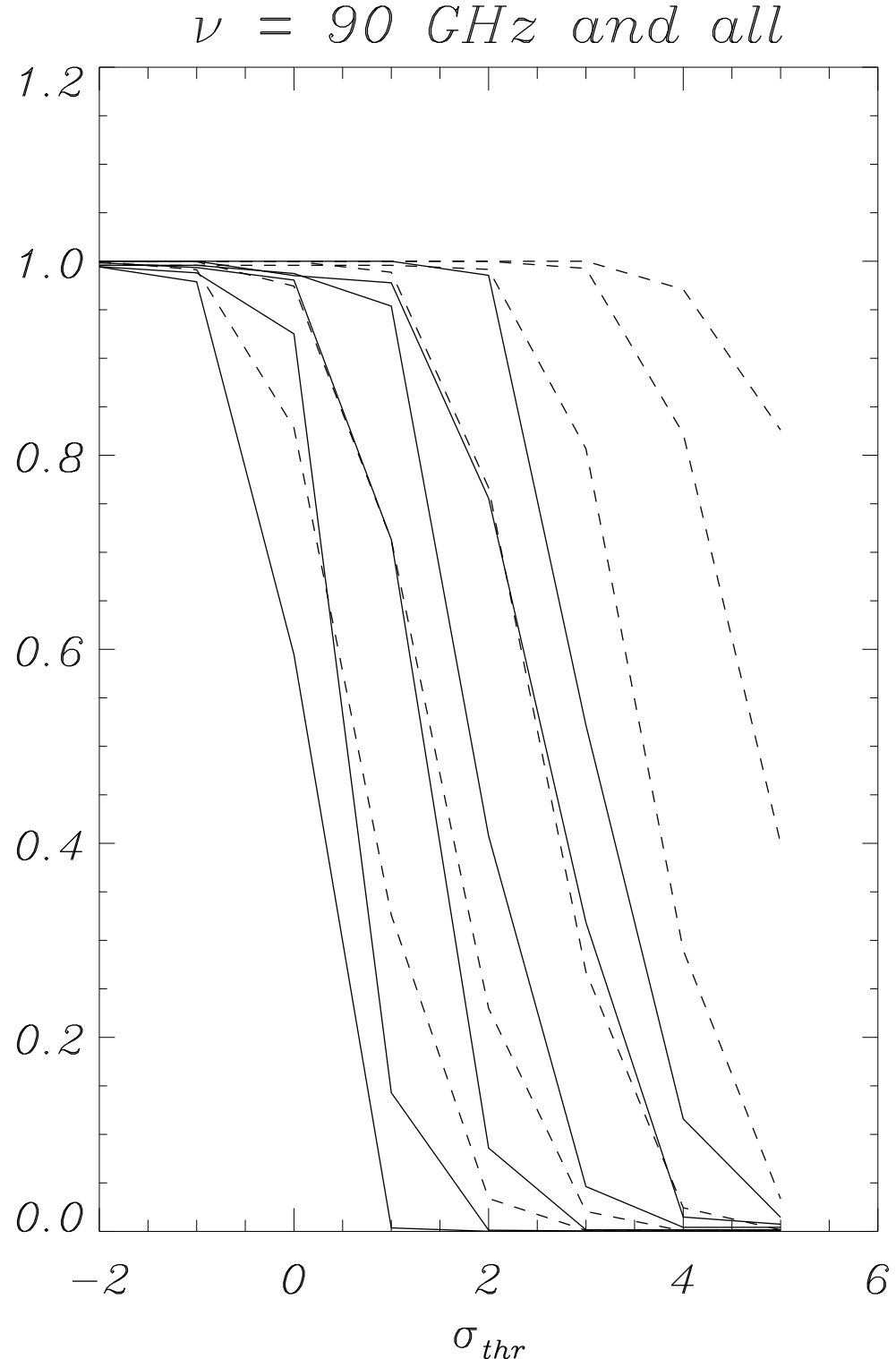


Fig. 3.— Fraction of sources found in the filtered 90 GHz map (dashed line) and in all maps (solid line) as a function of σ_{thr} (standard deviation of the filtered map). From left to right, the lines correspond to sources below 1 σ_{CMBn} , between 1 and 2, 2 and 3, 3 and 4, 4 and 5, 5 and 6.

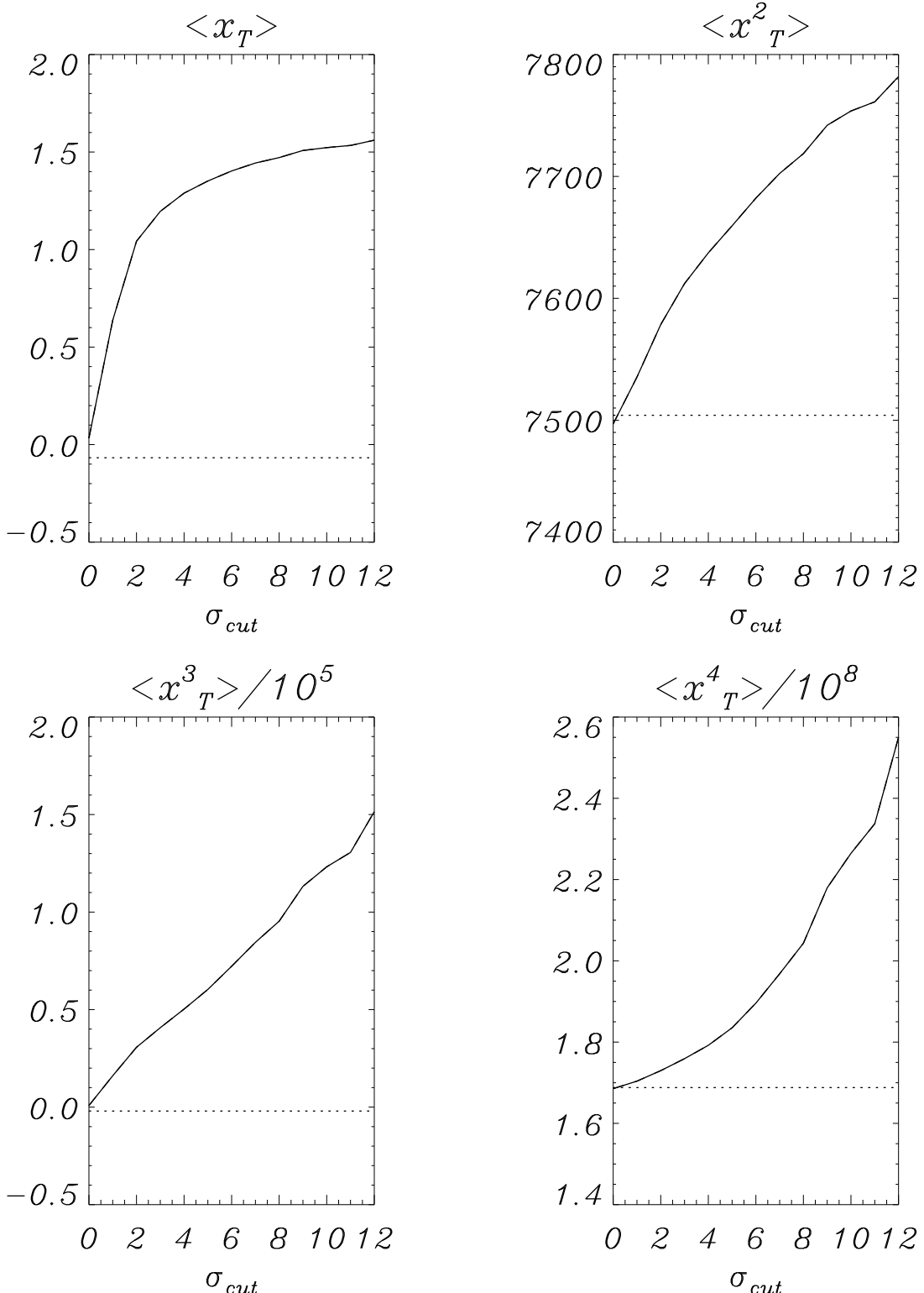


Fig. 4.— The first four moments of the 90 GHz observed map once point sources above σ_{cut} have been subtracted. The dotted and solid lines are the moments of the CMBn and observed maps respectively. The map is in Raleigh–Jeans temperature, the y axis units vary accordingly.

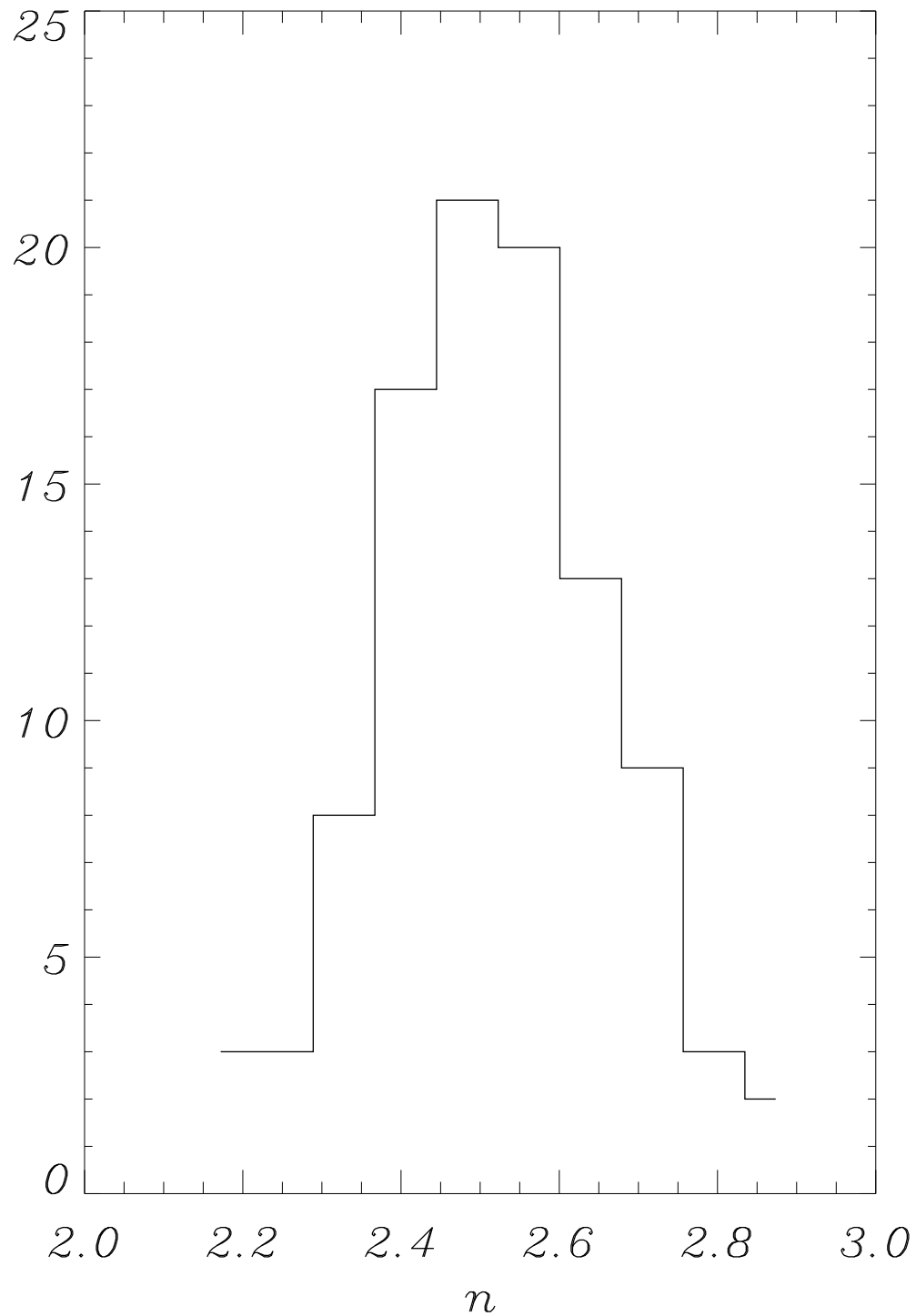


Fig. 5.— Histogram of the estimates of the slope of point sources n from the simultaneous fitting of all moments.

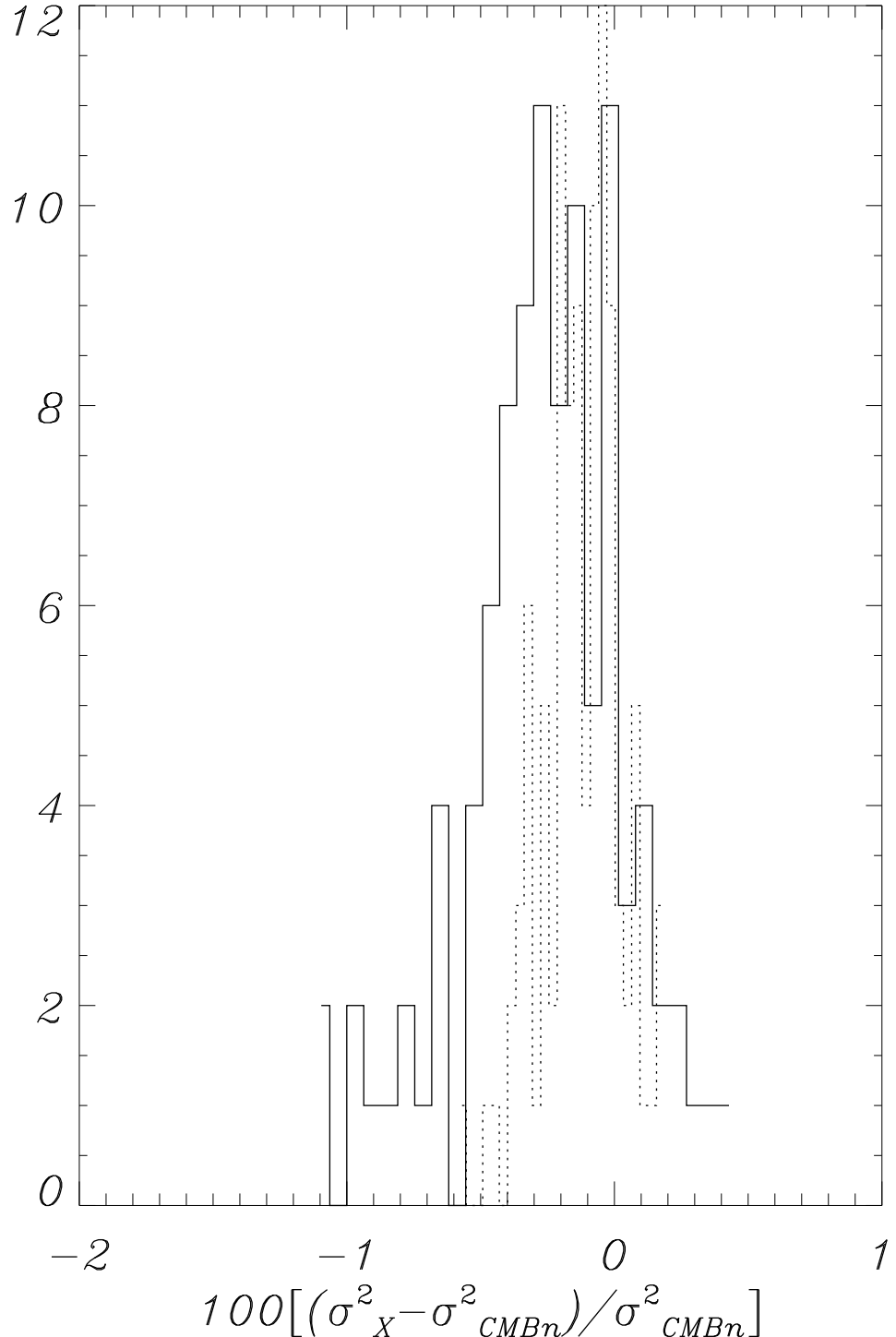


Fig. 6.— Histograms of the percentage differences between the estimated variance σ_X^2 and the input map value. The solid curve refers to best fit values for the n values that minimize the likelihood (fig. 5). The dotted histogram correspond to the σ_X^2 value obtained for a fixed $n = 2.5$. Both histograms are obtained fitting simultaneously all moments for $\sigma_{cut} \geq 4$.

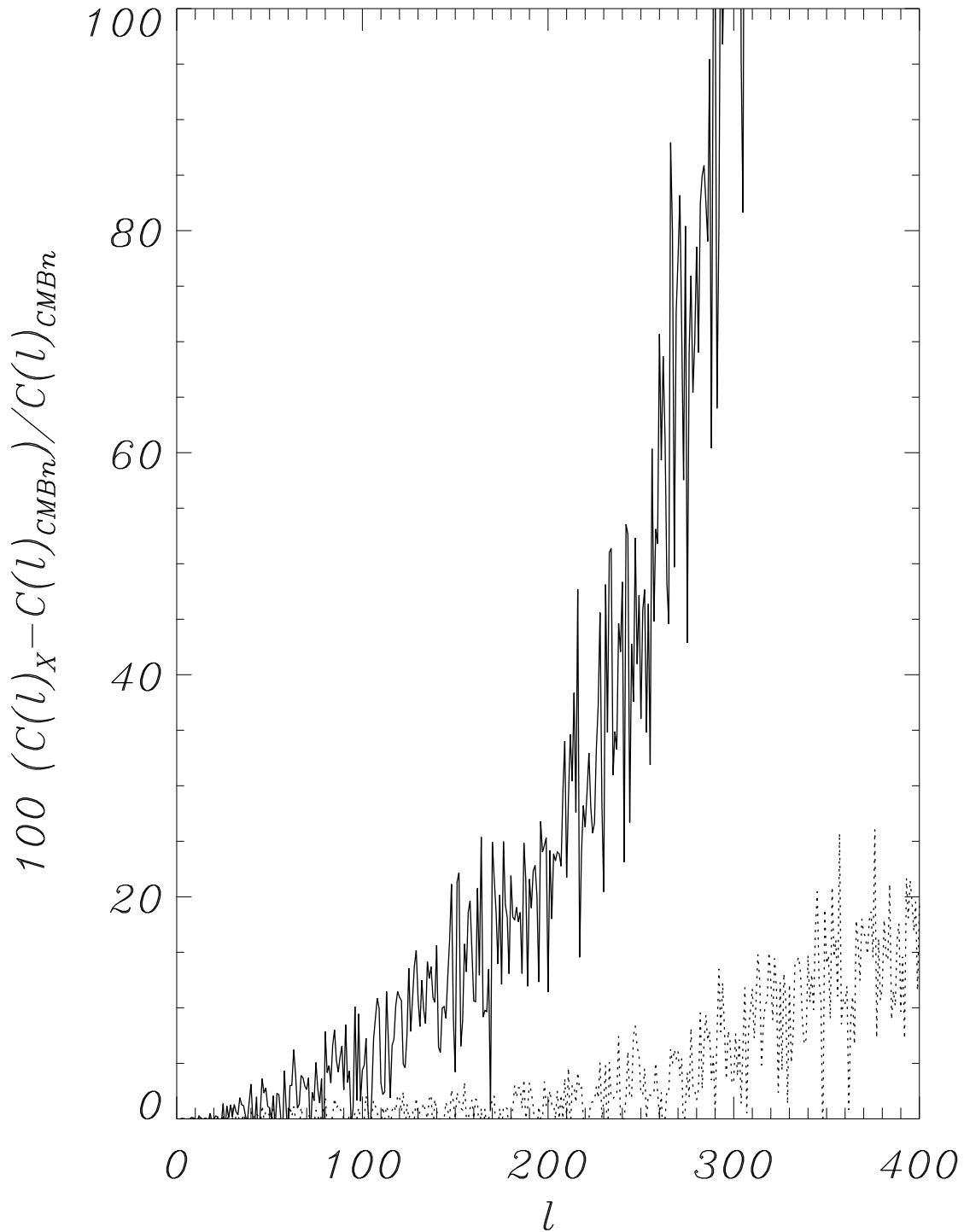


Fig. 7.— The percentage difference between the power spectrum computed from a 90 GHz CMBn map and the corresponding observed one with all point sources (solid line) and only sources below 4σ (dotted line).

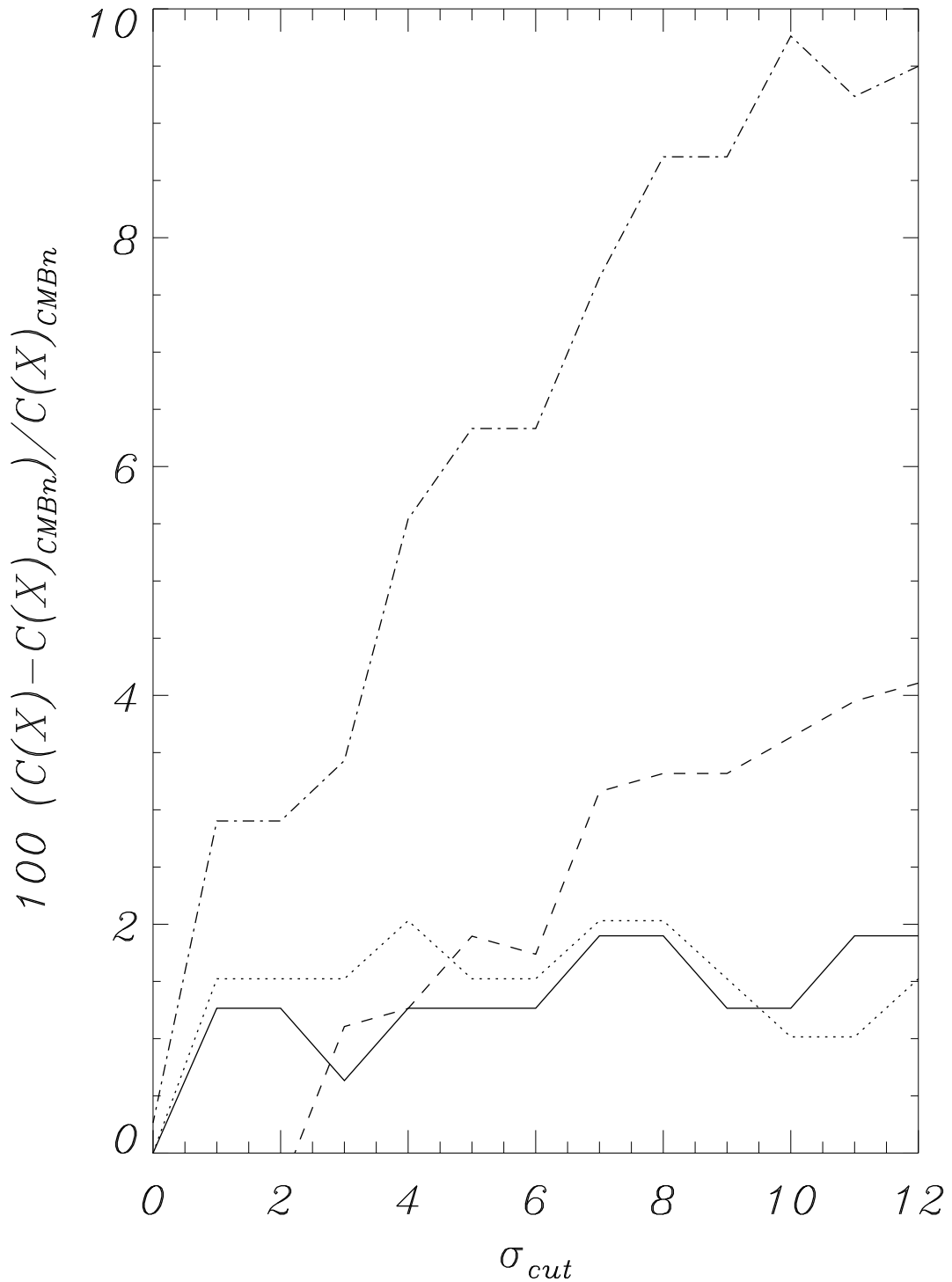


Fig. 8.— Percentage difference between the power spectra computed from the observed 90 GHz map (after progressive subtraction of point sources) and the underlying CMBn map. The different lines correspond to $l = X = 400$ (dot – dashed), 300(dashed), 200(solid) and 100(dotted).